

A Theoretical and Experimental Investigation of Hingeless-Rotor Stability and Trim*

S. Subramanian G. H. Gaonkar
 Research Associate Professor
 Department of Mechanical Engineering
 Florida Atlantic University
 Boca Raton, FL 33431, USA

T. H. Maier
 Research Scientist
 Army Aeroflightdynamics Directorate (AMCOM)
 Ames Research Center
 Moffett Field, CA 94035, USA

Abstract

The stability of an isolated hingeless rotor in forward flight is investigated, both experimentally and analytically. The test model has four soft-inplane and torsionally soft blades, and is tested at realistic tip speeds. The collective pitch and shaft angle are set prior to each test point, and the rotor is trimmed as follows: the longitudinal and lateral cyclic pitch controls are adjusted through a swashplate to minimize the 1/rev flapping moment at the 12% radial station. Key measurements in the database include the cyclic pitch controls, steady root-flap moment and lag regressive-mode damping for two coning angles with advance ratio, shaft angle and collective pitch variations. A modal approach, the ONERA dynamic stall models of lift, drag and pitching moment, and a three-dimensional state-space wake model are used. The cyclic pitch controls and the corresponding periodic responses are predicted by the periodic shooting method with damped Newton iteration; this method is based on the fast-Floquet theory and generates the equivalent Floquet transition matrix (EFTM) as a byproduct. The eigenvalues and eigenvectors of the EFTM lead to the frequencies and damping levels. All the structural and aerodynamic states are included from trim analysis to eigenanalysis. A major finding is that dynamic wake dramatically improves the correlation of the lateral cyclic pitch control.

Nomenclature

Unless otherwise stated, the symbols below are dimensionless:

a linear lift curve slope
 a_d, a_m damping factors in dynamic stall drag and pitching moment models
 b airfoil semi-chord, (divided by R)
 c airfoil chord, (divided by R)
 c_d, c_{d_0} airfoil drag coefficient and constant profile-drag coefficient

c_d quasisteady drag coefficient
 c_z, c_m airfoil lift and pitching moment coefficients
 c_{m_0} airfoil pitching moment coefficient at zero angle of attack
 c_{m_s} quasisteady pitching moment coefficient
 C_T thrust coefficient
 C_T/σ thrust level or blade loading
 c_{z_1} extrapolated linear-lift coefficient
 c_{z_s} quasisteady lift coefficient
 d dynamic-stall-lift damping parameter
 e phase shift parameter in dynamic stall lift model
 e_h hinge offset, (divided by R)
 E_d, E_m phase shift parameters in dynamic stall drag and pitching moment models
 g gravity
 I, J, K unit vectors associated with inertial frame XYZ
 i, j, k unit vectors associated with undeformed blade coordinate system xyz
 k_{m_1}, k_{m_2} mass radii of gyration of blade cross section about its principle axes
 ℓ blade span, $1 - e_h$, (divided by R)
 L_x, L_y sectional aerodynamic forces
 $\mathcal{L}_u, \mathcal{L}_w$ total horizontal and vertical forces
 m mass per unit length, (divided by m_r)
 m_r reference mass per unit length, (kg/m)
 M_ϕ aerodynamic pitching moment
 \mathcal{M}_v total pitching moment
 \mathcal{M} total flap moment at e_f , (divided by $\rho_\infty b \Omega^2 R^4$)
 \mathcal{M}_{nc} n -th harmonic cosine component of \mathcal{M}
 \mathcal{M}_{ns} n -th harmonic sine component of \mathcal{M}
 \mathcal{M}_0 steady component of \mathcal{M}
 N_{el} number of aerodynamic elements
 r_c root cutout, (divided by R)
 r_d, r_m frequency parameters in dynamic stall drag and pitching moment models
 \bar{r}_i radial station of the i -th blade, (divided by R)
 R rotor radius, (m)
 v inplane (lag) bending deflection, (divided by R)

* Paper presented at the 23rd European Rotorcraft Forum, Dresden, Germany, September 16-18, 1997.

w	dynamic stall lift frequency parameter; also out of plane (flap) bending deflection, (divided by R)
x	radial distance measured from the rotor center, (divided by R)
α	blade airfoil angle of attack
α_s	shaft angle, positive rearward, (<i>deg</i>)
$\alpha_{s,s}$	quasisteady stall angle, (<i>deg</i>)
β_{pc}	blade precone, (<i>deg</i>)
γ	Lock number (blade inertia parameter)
δ	pitch-rate coefficient
θ	blade pitch angle
θ_0	collective pitch angle, (<i>deg</i>)
θ_c, θ_s	lateral and longitudinal cyclic pitch angles, (<i>deg</i>)
λ	time-delay parameter
Λ_2	flap bending stiffness, (divided by $m_r \Omega^2 R^4$)
μ	advance ratio
σ	rotor solidity
ψ_i	azimuthal location of the i -th blade
ρ_∞	air density (kg/m^3)
Ω	rotor angular speed, (<i>rad/sec</i>)
$\zeta \omega_n$	lag regressive-mode damping level
$()$	time derivative of $()$
$()'$	spatial derivative of $()$

Introduction

The provision for adequate lead-lag damping is an important element of rotorcraft design; this requires an accurate prediction method. Since aerodynamic and inertial forces are delicately balanced in the in-plane direction, lag-damping prediction is sensitive to the approximations in modeling the aerodynamic and structural components such as wake and torsional dynamics. It is sensitive to the trim results as well; that is, to the control inputs and the corresponding periodic responses. Given this sensitivity, it is virtually imperative that the theoretical calculations are correlated with a comprehensive database from simplified models whose properties are accurately characterized. The present study addresses such calculations under wind-tunnel trim conditions as well as generation of a database and correlations. In particular, an isolated hingeless rotor with four blades is tested at realistic tip speeds; the blades are soft-inplane with a low torsional stiffness and are of simple airfoil and planform design. Compared to bearingless hubs and advanced-geometry blades, the design of the hub-flexure-blade assembly is far simpler (details to follow). This simplicity and the isolation of the body or rotor-support motions from the blade motions help keep the focus on aerodynamic aspects. To provide a better appreciation for this work, we begin with a mention of the related developments on isolated hingeless-rotor stability.

In the early '80s, McNulty experimentally investigated the stability of a soft-inplane hingeless rotor with three blades (Ref. 1). The collective pitch θ_0 , shaft angle α_s , and advance ratio μ were manually set prior to each test run; the model has no cyclic pitch control, and it was operated untrimmed. The strengths of the experiment were its structural simplicity and aerodynamically demanding conditions. In fact, the first torsion frequency was kept as high as possible, and the hub-flexure-blade assembly closely approximated the rigid flap-lag model with root restraint. Moreover, the database included dynamically stalled conditions with advance ratio as high as 0.55 and shaft angle as high as 20° . These strengths motivated many investigations right until today (Refs. 2–8) and helped isolate the nonlinear dynamic stall aspects of the stability problem. A case in point is a recent study by Chunduru *et al.* (Ref. 8) who correlate with nearly the complete database of Ref. 1 and review the aeroelastic stability studies through 1995. In this study (Ref. 8), the rigid flap-lag as well as elastic flap-lag-torsion representations are used, and the airfoil aerodynamics are represented by the ONERA dynamic stall models and the rotor wake by a three-dimensional finite-state wake model. The developments since 1995 include the works of de Andrade *et al.* (Ref. 9) and Cho *et al.* (Ref. 10), both on torsionally soft blades in the hovering conditions. In Ref. 9, the lag-damping predictions with a finite-state wake model are correlated with Sharpe's database (Ref. 11) and the wake is found to improve the correlation. Reference 10 is an analytical investigation based on a "large deflection-type beam theory" that does not involve an ordering scheme; that is, without kinematic limitations on the magnitude of displacements and rotations. Moreover, a three-dimensional unsteady vortex lattice method with a prescribed wake geometry is used to model the flow field. A major finding is that three-dimensional tip relief and wake dynamics significantly affect the stability predictions.

Despite the strengths, McNulty's experiment (Ref. 1) exhibited significant weaknesses as well. It was conducted at low tip speeds; the lack of a swashplate contributed to unrealistic flight conditions of negative thrust conditions for the bulk of the database; and no data are available to validate the predicted operational parameters such as thrust level or hub moment. To remove these weaknesses, the US Army Aeroflight-dynamics Directorate recently conducted experiments on isolated hingeless rotors in hover and forward flight (Ref. 12). Moreover, they also recognize the increasing need for a database on torsionally soft blades in trimmed flight. Thus, specifically stated, the primary objective is to generate a database on the trim and stability of a *torsionally soft rotor operating at realistic tip speeds* (Ref. 12). The rotor is trimmed with a conventional swashplate; specifically, the longitudinal

and lateral cyclic pitch controls are adjusted to minimize the 1/rev flap moment at the 12% radial station. The trim data of the cyclic pitch controls and steady root flap moment, and the stability data of the lag regressive-mode damping level are generated for two coning angles over a comprehensive range of collective pitch ($0^\circ \leq \theta_0 \leq 6^\circ$), shaft angle ($0^\circ \leq \alpha_s \leq 6^\circ$) and advance ratio ($0 \leq \mu \leq 0.36$). Reference 12 describes details of the experiments such as the model properties, test procedures and generation of the database that was still being updated, and it also includes correlations with the lag regressive-mode damping levels, primarily in hover. In this context, special mention must be made of two recent studies by Tang and Dowell (Refs. 13 and 14), who use a moving-block-type approach to predict the lag-damping levels and correlate with the data of Ref. 12. The dynamic inflow and ONERA dynamic stall models are used in Ref. 13, and in Ref. 14 the dynamic inflow model is replaced by a finite-state wake model. However, in both studies (Refs. 13 and 14), the rotor is untrimmed in the sense that the measured values of the lateral and longitudinal cyclic pitch controls are used. In particular, Ref. 14 shows that the finite-state wake model correlates better than the dynamic inflow model.

With this background, we spell out the contributions of this paper:

1. Updates the database of Ref. 12 as well as extends it to include an additional configuration with zero precone; see Table 1, which describes the five experimental test configurations for which calculations are shown. Also provides corrected information on cyclic pitch measurements of the database of Ref. 12.
2. Develops a flap-lag-torsion analysis based on the fast-Floquet theory (Ref. 6) to correlate with the database on trim and stability, and demonstrates the strengths and the weaknesses of the predictions.
3. Identifies the effects of quasisteady stall, dynamic stall and dynamic wake on trim and stability and shows how these effects participate in the correlation.

Experimental Rotor

The test model is a soft-inplane hingeless rotor with torsionally soft blades. The 7.5-ft diameter rotor has four blades of an NACA 0012 airfoil section with a 3.4-in chord. The blades have a rectangular planform with zero-degree pretwist and droop; see Fig. 1. The model also has a provision to vary the blade precone. The blade mass-center, tensile, aerodynamic and elastic axes are nearly coincident with the control axis, which is at the quarter-chord point. Table 2 summarizes the rotor properties of the experimental model.

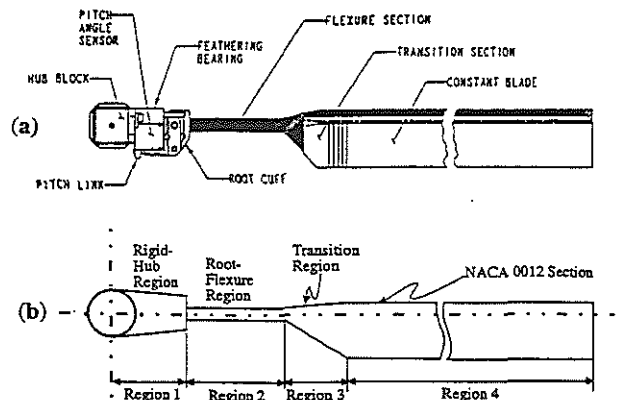


Figure 1: Hub-Flexure-Blade Assembly of the Experimental Rotor and Schematic

As seen from Fig. 1, the blade comprises four distinct regions. The first region is a hub section with very high stiffness values. The second region is a root-flexure section, which accommodates the blade flap and lead-lag motions. The third region is a short transition section

Table 1: Test Configurations for the Updated Database in Trimmed Flight

Test Configuration	Collective Pitch, θ_0 (deg)	Shaft tilt, α_s (deg)	Blade Precone β_{pc} (deg)	Advance Ratio, μ
a	3°	0°	2°	0.0–0.31
b	3°	-3°	2°	0.0–0.31
c	3°	-6°	2°	0.0–0.31
d	5.9°	-6°	2°	0.0–0.36
e	3°	0°	0°	0.0–0.187

tion, which is relatively stiff and provides transition from the blade root-flexure to the airfoil section. The fourth region is the NACA 0012 blade portion. Table 3 details the stiffness and mass distributions in each of these regions. The model is designed so that the test data correspond to the stability of an isolated rotor. The separation between the lag-regressive mode frequency and the lowest test-stand frequency is 7.1 Hz, which is far above the lag regressive-mode frequency. The collective pitch angle (θ_0) and shaft tilt angle (α_s) are set prior to each run and are known parameters. The rotor is operated trimmed with lateral and longitudinal cyclic pitch controls. The cyclic pitch controls are exercised through a conventional washplate mechanism that controls pitch on the blade root cuff at a location inboard of the flap-lag flexure motions (Fig. 1). The rotor is operated at 1700 rpm, which in hover gives a Reynolds number of 1.2×10^6 and

Mach number of 0.6 at the blade tip. In forward-flight tests, the shaft angle is set first and the rotor speed is brought up to the desired value. Then, the collective pitch is set, wind tunnel air speed is increased slowly to the desired forward-flight speed while the cyclic pitch controls are adjusted to maintain low-oscillatory flapping loads. When the desired forward-flight speed is reached, the collective pitch is readjusted to get the desired value and the cyclic pitch controls are further adjusted to minimize the 1/rev flapping moment at the 12% radial station. Then, low-amplitude cyclic excitation is applied. The frequency and magnitude of the excitation are adjusted so that the maximum lead-lag response (but below the structural limit) is attained. The excitation is shut off and the ensuing transient is recorded for 2 seconds. The recorded signals are analyzed using the moving-block analysis technique to obtain modal damping and frequency.

Table 2: Details of the Experimental Rotor

Number of blades	4
Airfoil section	NACA 0012
Hover blade-tip Mach number at 1700 rpm	0.6
Hover blade-tip Reynolds number at 1700 rpm	1.2×10^6
Rotor radius, ft	3.75
Blade chord, in	3.4
Nonrotating fundamental flap frequency, Hz	4.499
Nonrotating fundamental lead-lag frequency, Hz	14.405
Nonrotating fundamental torsion frequency, Hz	64.362
Blade precone, deg	0.0 and 2.0
Blade pretwist, deg	0.0
Blade droop, deg	0.0
Blade sweep, deg	0.0

Analysis

Elastic Flap-Lag-Torsion Equations

The flap-lag-torsion equations of motion are nonlinear partial differential equations, which are given in Ref. 6. A Galerkin-type scheme is used, which transforms these partial differential equations into a set of ordinary differential equations in terms of generalized coordinates. Orthogonal, nonrotating normal modes are used, which are developed by a Myklestad-type approach with identical mass and stiffness distributions of the experimental rotor; see Table 3. *In-vacuo* conditions are assumed and these modes are normalized with a tip deflection of one. As shown in Table 3, the stiffness distributions for the transition region (region 3) are not given because these distributions change continuously over this region and it was not possible

to measure them (Ref. 12). In the present correlation work, a linear variation for stiffness properties is assumed in the transition region while computing the mode shapes. Using these normal modes, the equations of motion are transformed into a set of modal equations in terms of the generalized coordinates. The Galerkin-type integrals associated with this transformation are evaluated numerically and also are given in Ref. 6. Moreover, the first two spatial derivatives of the mode shapes of bending deflections are computed from the slopes and bending moments, which are generated along with mode shapes in the Myklestad-type approach; for additional details, see Ref. 6.

Aerodynamics

The flow field is approximated by the dynamic stall and wake theory, which is a combination of the ONERA dynamic stall models for the airfoil lift, drag and pitching moment and a 3-D wake model for the rotor downwash (Refs. 15–17). This theory lends itself well to a finite-state representation and accounts for practically all the linear and nonlinear unsteady effects. In particular, the dynamic stall models include the effects of large angle of attack and reverse flow, and the wake model includes the effects of the finite number of blades, trailing vorticity and shed vorticity. Moreover, the lift and pitching-moment components associated with the apparent-mass effects are separately treated so as not to confuse them with the corresponding circulatory components. To help isolate the effects of dynamic stall and wake, we also approximate the flow field by the dynamic stall and quasisteady stall theories and include a mention of these three theories. This also shows explicitly the successively increasing degree of sophistication in approximating the flow field and the comprehensive aspect of the dynamic stall and wake theory.

Dynamic Stall Theory

According to this theory, the lift Γ_l , drag Γ_d and pitching moment Γ_m can be expressed as a combination of the linear and nonlinear or stalled components (Refs. 15 and 16):

$$\Gamma_l = \Gamma_{l_1} + \Gamma_{l_2}, \quad \Gamma_d = \Gamma_{d_1} + \Gamma_{d_2}, \quad \Gamma_m = \Gamma_{m_1} + \Gamma_{m_2} \quad (1)$$

These six components, two each in lift, drag and pitching moment, are given by Eqs. (2)–(4).

Lift:

$$k\dot{\Gamma}_{l_1} + \lambda\Gamma_{l_1} = \lambda a (U_y + b\dot{\epsilon}) \cos \alpha + \delta b\dot{\epsilon} \quad (2a)$$

$$\begin{aligned} k^2\ddot{\Gamma}_{l_2} &+ 2d\omega k\dot{\Gamma}_{l_2} + \omega^2(1+d^2)\Gamma_{l_2} \\ &= -\omega^2(1+d^2)[U\Delta c_z \\ &+ ek(\dot{U}_x \cos \alpha + \dot{U}_y \sin \alpha)\Delta c_z \\ &+ ek(\dot{U}_y \sin \alpha - \dot{U}_x \cos \alpha)\frac{\partial \Delta c_z}{\partial \alpha}] \end{aligned} \quad (2b)$$

Table 3: Structural Properties of the Experimental Rotor

Region	Radius r/R	Mass (slugs/ft)	Polar Inertia/ft (slugs-ft)	Flap stiffness (lbs-ft ²)	Lag stiffness (lbs-ft ²)	Torsion stiffness (lbs-ft ²)	Axial stiffness (lbs)
1	0.000-0.104	—	—	very high	very high	very high	very high
2	0.104-0.216	0.00575	2.42×10^{-6}	52.076	268.58	22.188	1.022×10^6
3	0.216-0.306	0.00981	4.12×10^{-5}	—	—	—	—
4	0.306-1.000	0.00633	3.57×10^{-5}	53.728	1698.90	26.395	4.796×10^5

Drag:

$$\Gamma_{d_1} = U c_{d_0} \quad (3a)$$

$$k^2 \ddot{\Gamma}_{d_2} + a_d k \dot{\Gamma}_{d_2} + r_d^2 \Gamma_{d_2} = - [r_d^2 U \Delta c_d + E_d k \dot{U}_y] \quad (3b)$$

Pitching Moment:

$$\Gamma_{m_1} = U c_{m_0} + \delta_m b \dot{\epsilon} \quad (4a)$$

$$k^2 \ddot{\Gamma}_{m_2} + a_m k \dot{\Gamma}_{m_2} + r_m^2 \Gamma_{m_2} = - [r_m^2 U \Delta c_m + E_m k \dot{U}_y] \quad (4b)$$

The algebraic structure of Eqs. (2a), (3a) and (4a) is revealing. In particular, the linear components Γ_{L_1} , Γ_{d_1} and Γ_{m_1} follow the classical thin-airfoil theory, and $\dot{\epsilon}$ in Eq. (2a) represents an airfoil rotation rate relative to airmass and includes complete geometric rotations of the airfoil. By comparison, the nonlinear components Γ_{L_2} , Γ_{d_2} and Γ_{m_2} are driven by Δc_z , Δc_d and Δc_m , respectively, which represent the differences between the corresponding linear and quasisteady-stall characteristics. They also involve the airfoil dynamic-stall characteristics. In the sequel, a brief account of these characteristics is given for an NACA 0012 airfoil.

For the quasisteady stall characteristics, we follow the measurements of Critzos *et al.* (Ref. 18) at a Reynolds number of 1.8×10^6 . In Ref. 3, Barwey *et al.* present analytical expressions to approximate the quasisteady-stall characteristics of an NACA 23012 airfoil. These expressions with some modifications for an NACA 23012 airfoil are used here. For the lift model, the quasisteady lift coefficient c_z , and extrapolated lift coefficient c_{z_1} are given by

$$c_{z_1} = a \sin \alpha \cos \alpha \quad 0^\circ \leq \alpha \leq 180^\circ \quad (5a)$$

$$c_{z_s} = c_{z_1} \quad 0^\circ \leq \alpha \leq \alpha_{s_s} \quad (5b)$$

$$c_{z_s} = a \sin \alpha_{s_s} \cos \alpha_{s_s} \quad \alpha_{s_s} < \alpha < 45^\circ \quad (5c)$$

$$c_{z_s} = a \sin \alpha_{s_s} \cos \alpha_{s_s} \sin 2\alpha \quad 45^\circ \leq \alpha \leq 135^\circ \quad (5d)$$

$$c_{z_s} = -a \sin \alpha_{s_s} \cos \alpha_{s_s} \quad 135^\circ < \alpha < 166^\circ \quad (5e)$$

$$c_{z_s} = c_{z_1} \quad 166^\circ \leq \alpha \leq 180^\circ \quad (5f)$$

where $a = 6.28$ and $\alpha_{s_s} = 14^\circ$.

For the drag model, the quasisteady drag coefficient c_{d_s} and the constant drag coefficient c_{d_0} are:

$$c_{d_0} = 0.01 \quad (6a)$$

$$c_{d_s} = 1.05 - (1.05 - c_{d_0}) \cos 2\alpha \quad 0^\circ \leq \alpha \leq 360^\circ \quad (6b)$$

For the pitching moment model, the quasisteady moment coefficient c_{m_s} is given by

$$c_{m_s} = c_{m_0} \quad 0^\circ \leq \alpha \leq \alpha_{s_s} \quad (7a)$$

$$c_{m_s} = c_{m_0} - 0.0582257 \tan^{-1}(\alpha - \alpha_{s_s}) \quad \alpha_{s_s} < \alpha \leq 20^\circ \quad (7b)$$

$$c_{m_s} = c_{m_0} - 0.55 \sin(\alpha - 20^\circ) - 0.0842201 \cos(\alpha - 20^\circ) \quad 20^\circ < \alpha \leq 101.2941^\circ \quad (7c)$$

$$c_{m_s} = c_{m_0} - 0.55641 \cos[0.75(\alpha - 101.2941^\circ)] \quad 101.2941^\circ < \alpha \leq 170^\circ \quad (7d)$$

$$c_{m_s} = 0.3461497[0.1(\alpha - 170^\circ)] \quad 170^\circ < \alpha \leq 180^\circ \quad (7e)$$

where $c_{m_0} = 0.0$. Figure 2 shows the variations of the quasisteady lift, drag and pitching moment coefficients. It also includes a comparison with the test data from Ref. 18 and with the extrapolated linear-lift coefficient c_{z_1} according to Eq. (5a).

The dynamic stall parameters in Eqs. (2)–(4) are identified on the basis of wind-tunnel experiments; these are λ , δ , d , e and w in the lift equation, a_d , r_d and E_d in the drag equation and δ_m , a_m , r_m and E_m in the

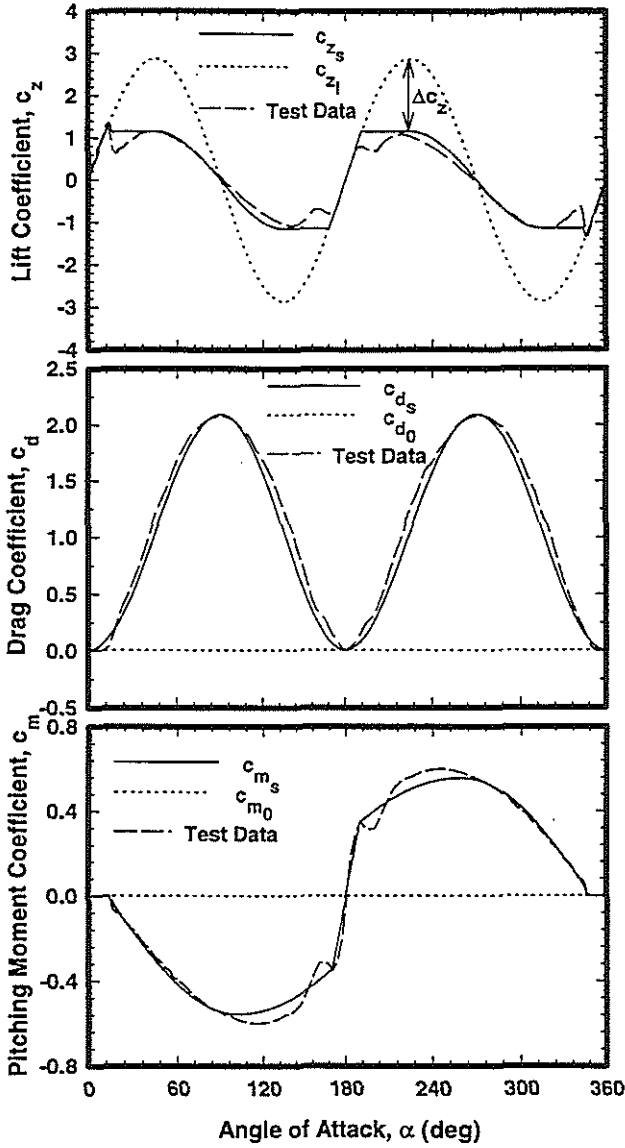


Figure 2: Variation of Airfoil Lift, Drag and Pitching Moment Coefficients for an NACA 0012 Airfoil Section

pitching-moment equation. Following earlier studies (e.g., Ref. 13), we use the following expressions for these parameters:

$$\lambda = 0.15 \quad (8a)$$

$$\delta = \frac{\partial c_{z_1}}{\partial \alpha} - \frac{a}{2} \quad (8b)$$

$$w^2(1 + d^2) = [0.2 + 0.1(\Delta c_z)^2]^2 \quad (8c)$$

$$2dw = 0.25 + 0.1(\Delta c_z)^2 \quad (8d)$$

$$e = -0.6(\Delta c_z)^2 \quad (8e)$$

$$a_d = 0.32 \quad (9a)$$

$$r_d = 0.2 + 0.1(\Delta c_z)^2 \quad (9b)$$

$$E_d = -0.015(\Delta c_z)^2 \quad (9c)$$

$$a_m = 0.25 + 0.1(\Delta c_z)^2 \quad (10a)$$

$$r_m = 0.2 + 0.1(\Delta c_z)^2 \quad (10b)$$

$$E_m = -0.6(\Delta c_z)^2 \quad (10c)$$

Now, concerning the apparent-mass terms L_0 and M_0 , we separate them from the circulatory terms (Ref. 15). This is conveniently done in the local airfoil coordinates shown in Fig. 3, and the corresponding lift components L_x and L_y , and pitching moment M can be expressed as

$$L_y = U_x[\Gamma_{t_1} + \Gamma_{t_2}] + U_y[\Gamma_{d_1} + \Gamma_{d_2}] + L_0 \quad (11a)$$

$$L_x = -U_y[\Gamma_{t_1} + \Gamma_{t_2}] + U_x[\Gamma_{d_1} + \Gamma_{d_2}] \quad (11b)$$

$$M = 2b[U(\Gamma_{m_1} + \Gamma_{m_2})] + M_0 \quad (11c)$$

In Eqs. (11a) and (11c), L_0 and M_0 represent apparent mass lift normal to the chord and noncirculatory pitching moment, both at the three-quarter chord point, and are given by

$$L_0 = bs \left[\dot{U}_y + \frac{1}{2} b \ddot{\epsilon} \right] \quad (11d)$$

$$M_0 = 2b^2 [\delta_m \dot{U}_y + s_m b \ddot{\epsilon}] \quad (11e)$$

where s and s_m are apparent mass parameter and non-circulatory pitching moment parameter, respectively. For later reference, we also introduce the blade sectional circulatory lift L_i :

$$L_i = U(\Gamma_{t_1} + \Gamma_{t_2}) \quad (11f)$$

Quasisteady Stall Theory

According to this theory, we include only the quasisteady stall effects by considering the airfoil-section quasisteady stall characteristics. Equations (12a)–(12c) are obtained by suppressing the dynamic stall characteristics in Eqs. (2)–(4); that is,

$$\Gamma_{t_1} = a(U_y + b\dot{\epsilon}) \cos \alpha; \quad \Gamma_{t_2} = -U\Delta c_z \quad (12a)$$

$$\Gamma_{d_1} = U c_{d_0}; \quad \Gamma_{d_2} = -U\Delta c_d \quad (12b)$$

$$\Gamma_{m_1} = U c_{m_0} + \delta_m b \dot{\epsilon}; \quad \Gamma_{m_2} = -U\Delta c_m \quad (12c)$$

Dynamic Stall and Wake Theory

This is the baseline theory, which represents a combination of the dynamic stall theory and a three-dimensional finite-state wake theory of Peters, Boyd and He (Ref. 17). At a radial station \bar{r}_i and azimuth position ψ_i , the instantaneous wake or downwash $\lambda(\bar{r}_i, \psi_i, t)$ is given by a complete set of radial shape functions $\phi_j^r(\bar{r}_i)$ and spatial harmonics $\cos(r\psi_i)$ and $\sin(r\psi_i)$:

$$\lambda(\bar{r}_i, \psi_i, t) = \sum_{r=0}^{\infty} \sum_{j=r+1, r+3}^{\infty} J_0(\tau k) \phi_j^r(\bar{r}_i) [\alpha_j^r(t) \cos(r\psi_i) + \beta_j^r(t) \sin(r\psi_i)] \quad (13)$$

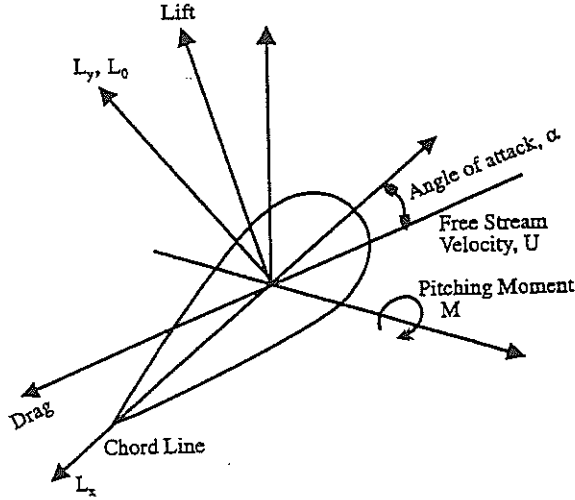


Figure 3: Schematic of Airfoil-Section Aerodynamics

where the cosine component $\alpha_j^r(t)$ and the sine component $\beta_j^r(t)$ are the wake states. These states are given by

$$M \{ \dot{\alpha}_j^r \} + V L_c^{-1} \{ \alpha_j^r \} = 0.5 \{ \tau_n^{mc} \} \quad (14a)$$

$$M \{ \dot{\beta}_j^r \} + V L_s^{-1} \{ \beta_j^r \} = 0.5 \{ \tau_n^{ms} \} \quad (14b)$$

where V is the diagonal matrix with $V_{11} = V_t = \sqrt{(\mu^2 + \lambda_t^2)}$ and all other elements are given by $V = [\mu^2 + (\lambda_t + \lambda_m) \lambda_t] / \sqrt{(\mu^2 + \lambda_t^2)}$. A noteworthy feature is that the closed-form expressions are available for the diagonal mass matrix M and influence coefficient matrices L_c and L_s . Similarly, τ_n^{mc} and τ_n^{ms} are cosine and sine components of the pressure coefficient, which, for a rotor with Q blades simplify to (Ref. 17)

$$\tau_n^{oc} = \frac{1}{2\pi} \sum_{i=1}^Q \int_0^1 \frac{L_i \phi_n^0(\bar{r}_i)}{\rho \Omega^2 R^3} d\bar{r}_i; \quad (15a)$$

$$\tau_n^{mc} = \frac{1}{\pi} \sum_{i=1}^Q \int_0^1 \frac{J_0(mk) L_i \phi_n^m(\bar{r}_i)}{\rho \Omega^2 R^3} d\bar{r}_i \cos(m\psi_i); \quad (15b)$$

$$\tau_n^{ms} = \frac{1}{\pi} \sum_{i=1}^Q \int_0^1 \frac{J_0(mk) L_i \phi_n^m(\bar{r}_i)}{\rho \Omega^2 R^3} d\bar{r}_i \sin(m\psi_i); \quad (15c)$$

where L_i is the sectional circulatory lift given by Eq. (11f), J_0 the Bessel function of the first kind of order zero, and $k = \frac{b}{\bar{r}_i}$. Since rotor blades have high aspect ratio, J_0 can be set to unity (Ref. 8). We particularly emphasize that in the dynamic stall and wake theory, the Γ_{t_1} term in Eq. (2a) is deleted. This is because it is a one-pole approximation to Theodorsen's wake and the wake is completely accounted for in the three-dimensional wake model typified by Eqs. (13)–(15c); for details see Ref. 8. The computation of equilibrium-state inflow is based on the momentum theory in the quasisteady stall and dynamic stall theories, and on the coupled blade-wake-stall equations in the dynamic stall and wake theory.

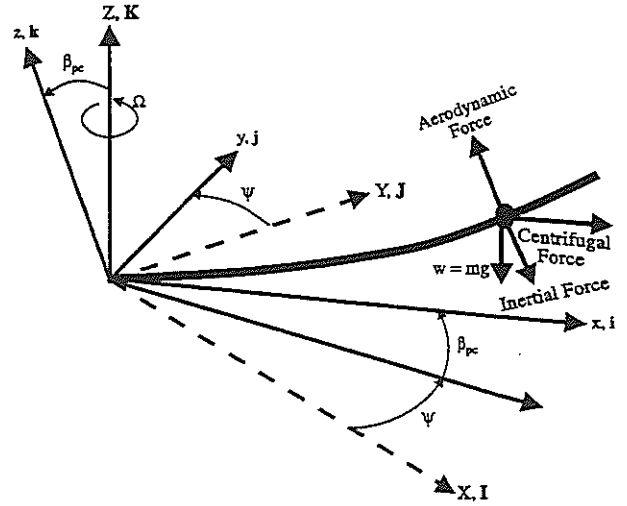


Figure 4: Blade Coordinate Systems and Sectional Forces

Trim Analysis

For the test model the collective pitch and shaft angle are known control inputs. Therefore, trim analysis per se refers to finding the lateral and longitudinal cyclic control inputs by minimizing 1/rev flap moment at the 12% radial station and to finding the corresponding initial conditions for the periodic responses. The shooting method with damped Newton iteration is used; it is based on the fast-Floquet theory and generates the equivalent Floquet transition matrix (EFTM) as a byproduct. The modal damping levels and frequencies are obtained from the eigenvalues and eigenvectors of the EFTM; for details see Ref. 6. The analysis still requires two additional trim equations that satisfy the required trim conditions of minimized 1/rev flap moment at 0.12R. For completeness we include a brief account of the trim equations.

Flap Moment Equations

Consider a generic material point on the blade at a radial location x from the hinge offset. As shown in Fig. 4, the generic point is subjected to inertial, aerodynamic, centrifugal and gravitational forces. It is expedient to express the components of each of these forces in the undeformed blade coordinate system xyz . Let \mathcal{L}_u and \mathcal{L}_w represent the total horizontal and vertical forces (excluding gravitational force) parallel and perpendicular to the undeformed x -coordinate, respectively. Similarly, let \mathcal{M}_y represent the total moment acting parallel to the undeformed y -coordinate and let e_f represent the 12% radial location about which the flap moment is computed. Following Ref. 19, we predict the flap moment by the force-integration approach, in which the integration of the sectional forces and moments over the blade span leads to the total

moment. Therefore, the total flap moment is given by

$$\mathcal{M}(e_f, \psi) = \int_{e_f}^{\ell} \{ \mathcal{L}_u [w(x) - w(e_f)] - (\mathcal{L}_w - mg)(x - e_f) + \mathcal{M}_v \} dx \quad (16)$$

Now, we express the forces and moment in Eq. (16) as a sum of inertial and aerodynamic components. The inertial component includes contribution from the centrifugal forces as well; that is,

$$\mathcal{L}_u = \mathcal{L}_u^I + \mathcal{L}_u^A, \quad \mathcal{L}_w = \mathcal{L}_w^I + \mathcal{L}_w^A, \quad \mathcal{M}_v = \mathcal{M}_v^I + \mathcal{M}_v^A \quad (17)$$

where the superscripts *I* and *A* indicate that the contributions are of inertial and aerodynamic origin. Substituting Eq. (17) in Eq. (16), we get

$$\begin{aligned} \mathcal{M}(e_f, \psi) &= \int_{e_f}^{\ell} \{ \mathcal{L}_u^I [w(x) - w(e_f)] \\ &\quad - \mathcal{L}_w^I (x - e_f) + \mathcal{M}_v^I \} dx \\ &\quad + \int_{e_f}^{\ell} \{ \mathcal{L}_u^A [w(x) - w(e_f)] \\ &\quad - \mathcal{L}_w^A (x - e_f) + \mathcal{M}_v^A \} dx \\ &\quad + \int_{e_f}^{\ell} mg(x - e_f) dx \\ &= \mathcal{M}^I(e_f) + \mathcal{M}^A(e_f) \\ &\quad + \int_{e_f}^{\ell} mg(x - e_f) dx \end{aligned} \quad (18)$$

The expressions for sectional inertial forces, \mathcal{L}_u^I and \mathcal{L}_w^I , are derived from the Newton's second law:

$$\mathcal{L}^I = \mathcal{L}_u^I \mathbf{i} + \mathcal{L}_w^I \mathbf{j} + \mathcal{L}_k^I \mathbf{k} = - \iint \rho_s \mathbf{a} d\eta d\xi \quad (19)$$

where ρ_s and \mathbf{a} represent the material mass density and acceleration vector, respectively. Substituting for the blade acceleration relative to an inertial frame and performing the cross-sectional integrals, we get (Ref. 6)

$$\mathcal{L}_u^I = -\frac{6a}{\gamma} [-2m\dot{v} - m(x + e_h) + \beta_{pc}mw] \quad (20)$$

$$\mathcal{L}_w^I = -\frac{6a}{\gamma} [m\ddot{w} + 2\beta_{pc}m\dot{v} + \beta_{pc}m(x + e_h)] \quad (21)$$

In the derivation of the above equations, the influence of the axial deformation is neglected.

Similarly, the sectional inertial moments can be derived from

$$\begin{aligned} \mathcal{M}^I &= \mathcal{M}_u^I \mathbf{i} + \mathcal{M}_v^I \mathbf{j} + \mathcal{M}_k^I \mathbf{k} \\ &= - \iint \rho_s \mathbf{s} \times \mathbf{a} d\eta d\xi \end{aligned} \quad (22)$$

where \mathbf{s} represents the moment arm (Ref. 6). Substituting for \mathbf{s} and \mathbf{a} and performing the cross-sectional integrals, we get

$$\mathcal{M}_v^I = -\frac{6a}{\gamma} [-m\dot{v}' + mv']$$

$$\begin{aligned} &\{ (k_{m_2}^2 - k_{m_1}^2) \sin \theta \cos \theta \} \\ &- \frac{6a}{\gamma} [-m\dot{w}' + 2m\dot{\theta}' + mw' + m\beta_{pc}] \\ &\{ k_{m_2}^2 \sin^2 \theta + k_{m_1}^2 \cos^2 \theta \} \end{aligned} \quad (23)$$

Similarly, substitution of Eqs. (20), (21) and (23) for the inertial part into Eq. (18) gives

$$\begin{aligned} \mathcal{M}^I(e_f, \psi) &= \frac{6a}{\gamma} \int_{e_f}^{\ell} \{ 2m\dot{v} [w(x) - w(e_f)] \\ &\quad + m(x + e_h) [w(x) - w(e_f)] \\ &\quad - \beta_{pc}mw [w(x) - w(e_f)] \\ &\quad + m\dot{w}(x - e_f) \\ &\quad + 2\beta_{pc}m\dot{v}(x - e_f) \\ &\quad + \beta_{pc}m(x - e_f)(x + e_h) \\ &\quad + mk_{m_2}^2 \dot{v}' \sin \theta \cos \theta \\ &\quad - mk_{m_2}^2 v' \sin \theta \cos \theta \\ &\quad + mk_{m_2}^2 \dot{w}' \sin^2 \theta - mk_{m_2}^2 w' \sin^2 \theta \\ &\quad - 2\dot{\theta}' mk_{m_2}^2 \sin^2 \theta \\ &\quad - mk_{m_2}^2 \beta_{pc} \sin^2 \theta \} dx \end{aligned} \quad (24)$$

The aerodynamic contribution to flap moment is obtained from the sectional aerodynamic forces and moments, which are calculated at the midpoint of each aerodynamic element. Hence, we use a discretized force-summation scheme instead of a continuous integration of the forces and moments along the length of the blade. Thus, in terms of sectional aerodynamic forces and moments, the flap moment due to aerodynamic forces can be expressed as

$$\begin{aligned} \mathcal{M}^A(e_f, \psi) &= \sum_{n=1}^{N_{el}} [\mathcal{L}_u^A \{ w(x_f) - w(e_f) \} \\ &\quad - \mathcal{L}_w^A x_f + \mathcal{M}_v^A]_n \Delta x_n \end{aligned} \quad (25)$$

In the above equation, x_{f_n} represents the radial distance of the midpoint from the 12% radial station, and Δx_n is the length of the *n*-th aerodynamic element. Expressing Eq. (25) in terms of sectional aerodynamic forces and moments, we get

$$\mathcal{L}_u^A = - (v' L_v + w' L_w) \quad (26)$$

$$\mathcal{L}_w^A = L_w \quad (27)$$

$$\mathcal{M}_v^A = v' M_\phi \quad (28)$$

where L_v , L_w and M_ϕ are the sectional aerodynamic forces and moments described in Ref. 6. Similarly, substitution of Eqs. (26)–(28) into Eq. (25) gives

$$\begin{aligned} \mathcal{M}^A(e_f, \psi) &= \sum_{n=1}^{N_{el}} [- (v' L_v + w' L_w) [w(x_f) - w(e_f)] \\ &\quad - L_w x_f + v' M_\phi]_n \Delta x_n \end{aligned} \quad (29)$$

Thus, substituting Eqs. (24) and (29) in Eq. (18) we get the flap moment expression.

Trim Equations

The total flap moment $\mathcal{M}(e_f, \psi)$ acting at the 12% radial station e_f is given by Eq. (18). To obtain its 1/rev components, we expand it in terms of Fourier series:

$$\mathcal{M}(e_f, \psi) = \mathcal{M}_0 + \sum_{n=1}^{\infty} [\mathcal{M}_{nc} \cos(n\psi) + \mathcal{M}_{ns} \sin(n\psi)] \quad (30)$$

For $n = 1$, we get

$$\mathcal{M}(e_f, \psi) = \mathcal{M}_0(e_f) + \mathcal{M}_{1c}(e_f) \cos \psi + \mathcal{M}_{1s}(e_f) \sin \psi \quad (31)$$

where

$$\mathcal{M}_{1c}(e_f) = \frac{1}{\pi} \int_0^{2\pi} \mathcal{M}(e_f, \psi) \cos \psi \, d\psi \quad (32)$$

$$\mathcal{M}_{1s}(e_f) = \frac{1}{\pi} \int_0^{2\pi} \mathcal{M}(e_f, \psi) \sin \psi \, d\psi \quad (33)$$

Therefore, the required trim conditions are

$$\mathcal{M}_{1c}(e_f) = \frac{1}{\pi} \int_0^{2\pi} \mathcal{M}(e_f, \psi) \cos \psi \, d\psi = 0 \quad (34)$$

$$\mathcal{M}_{1s}(e_f) = \frac{1}{\pi} \int_0^{2\pi} \mathcal{M}(e_f, \psi) \sin \psi \, d\psi = 0 \quad (35)$$

Thus, Eqs. (34) and (35) represent the trim equations, which are solved together with the response-periodicity conditions.

Mode Deflection Method

Concomitant to the force-integration method, the steady flapping moment at the radial location e_f is also estimated by the mode deflection method. That is;

$$\mathcal{M}(e_f, \psi) = [\Lambda_2(x)w''(x, \psi)]_{x=e_f} \quad (36)$$

where Λ_2 is the flap stiffness at radial station e_f . Moreover, w'' is evaluated from the second derivative of the mode shape, which comes out as a byproduct of the Myklestad approach. Therefore, the steady flap moment is given by

$$\mathcal{M}_0(e_f) = \frac{1}{2\pi} \int_0^{2\pi} \mathcal{M}(e_f, \psi) \, d\psi \quad (37)$$

Comparison with Experiment

Comparisons with experimental measurements include the lag regressive-mode damping level, control settings of lateral and longitudinal pitch angles and, finally, the steady root flap moment at the 12% radial station. The database refers to the five configurations identified in Table 1. Other details of the

test model are given in Tables 2 and 3. The calculations are based on the quasisteady stall, dynamic stall, and dynamic stall and wake theories and on a 5-5-5 modal representation; that is, five modes each in flap bending, lag bending and torsion. A few comparisons are made with the calculations from a 6-6-6 modal representation as reference or converged values. The two modal representations gave virtually identical values of damping level, control settings and root flap moment from the force-integration method. However, for the flap moment from the mode-deflection method, they gave differing values, which are spelled out while presenting the results. Blade weight is included in the flap-moment calculations; its effect on the calculations of damping levels and control settings is found to be negligible. Moreover, the measured structural lag damping of 0.5% is also included in the calculations. The thrust level C_T/σ , which is often mentioned in the sequel, is based on the dynamic stall and wake theory. Although no measurements of thrust-level, C_T/σ , are available, the flap-moment correlation provides an indirect means of validating the C_T/σ results.

Figure 5 shows the lag regressive-mode damping level versus advance ratio for the first three configurations with the same collective pitch $\theta_0 = 3^\circ$ and precone $\beta_{pc} = 2^\circ$ but with different shaft angles: $\alpha_s = 0^\circ, -3^\circ$ and -6° . As seen from the data, the damping level increases slowly with increasing advance ratio, reaches a maximum at a certain advance ratio, and thereafter decreases. Thus, the data exhibit a convex trend of damping variation with μ . Moreover, the data also show that once a maximum value is reached, the rate of decrease of damping with advance ratio increases with increasing shaft angle. For example, for the second configuration with $\alpha_s = -3^\circ$ in Fig. 5b, the maximum damping level of 1.04 (1/sec) occurs around $\mu = 0.15$, which is about 1.95% ($\zeta\omega_n = 5.842 \times 10^{-3}$) critical, and reduces to 1.27% critical at $\mu = 0.31$, a 35% reduction relative to the maximum. By comparison, the third configuration with $\alpha_s = -6^\circ$ in Fig. 5c, which has a maximum damping level of 1.65% critical at $\mu = 0.1$ becomes almost unstable at $\mu = 0.31$, a 92% reduction. Overall, the calculations from the quasisteady stall and dynamic stall theories are nearly identical and the minor differences between them are due to linear unsteady lift effects. This is expected since the maximum thrust level C_T/σ hardly exceeds 0.03 for all three configurations. To illustrate further, we once again consider the second configuration; the thrust level C_T/σ is 0.01 in hover, increases to 0.022 at $\mu = 0.15$ and thereafter decreases to 0.013 at $\mu = 0.31$. The calculations from the dynamic stall and wake theory are fairly close to those from the other two theories. Given the low thrust conditions, this is expected as well. The differences between the dynamic stall and dynamic stall and wake theories for $\mu < 0.15$ are due to dynamic wake effects; though not substan-

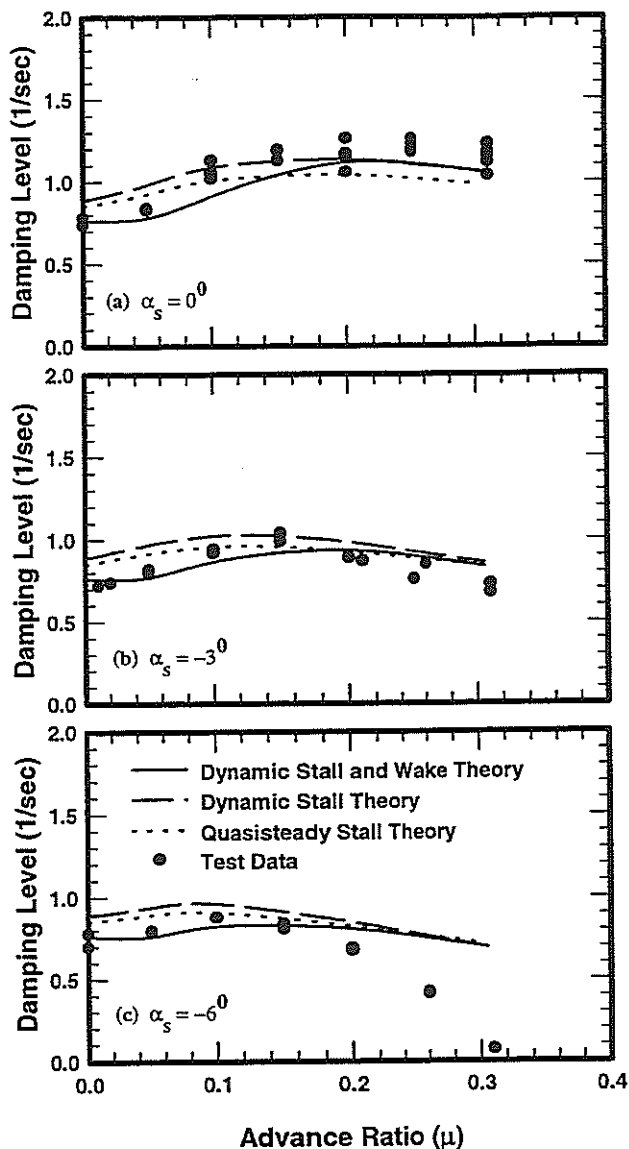


Figure 5: Lag Regressive-Mode Damping Correlation for $\theta_0 = 3^\circ$ and $\beta_{pc} = 2^\circ$

tial, they help improve the correlation in that they bring the calculations closer to the test data, specifically for $\mu < 0.2$. In particular, the dynamic stall and wake theory predicts slight increase in damping for $0 \leq \mu \leq 0.05$. For $\mu \geq 0.2$, it gradually merges with the other two theories as the low thrust level decreases still further with increasing advance ratio. Overall, all three theories show good correlation with the data except for the third configuration for $\mu > 0.2$; the thrust level (C_T/σ) is close to 0.015 at $\mu = 0.2$ and decreases with increasing advance ratio; in fact, it is zero for $\mu = 0.31$. According to the data, the damping level rapidly decreases and the lag regressive mode becomes nearly unstable at $\mu = 0.31$. None of the three theories captures this trend accurately. The

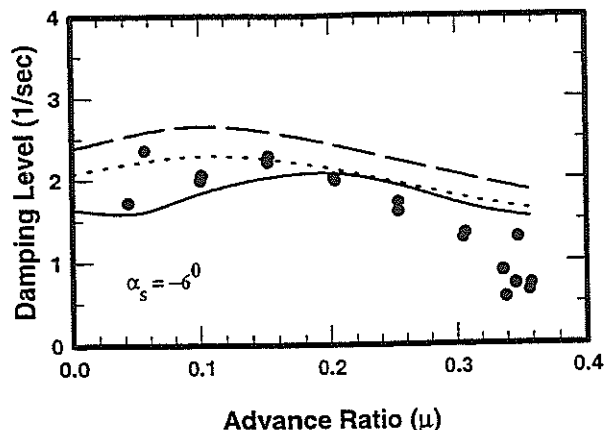


Figure 6: Lag Regressive-Mode Damping Correlation for $\theta_0 = 5.9^\circ$ and $\beta_{pc} = 2^\circ$ (Legend as in Fig. 5)

calculations show that the damping level is decreasing slowly with increasing advance ratio to a value of 1.3% critical at $\mu = 0.31$ where the data show neutral stability. That the correlation is unsatisfactory at near-zero thrust conditions is surprising, and investigation is continuing.

Figure 6 shows the comparison of measured and calculated damping levels for the fourth configuration with $\theta_0 = 5.9^\circ$, $\beta_{pc} = 2^\circ$ and $\alpha_s = -6^\circ$, and the data are available from a near-hovering condition at $\mu = 0.04$ to a fairly high-speed condition at $\mu = 0.36$. Despite some data scattering around $\mu = 0.05$ and 0.35 , the data show that the lag damping level increases for $0.04 \leq \mu \leq 0.15$ and decreases for $\mu > 0.15$. We also mention that the thrust level increases from 0.034 in hover to a maximum of 0.045 at $\mu \approx 0.1$ and thereafter decreases to 0.02 at $\mu = 0.36$. Overall, all three theories capture the trend of the data. However, the dynamic stall theory and to some extent the quasisteady stall theory overpredict the damping levels. The differences between the quasisteady stall and dynamic stall theories are mainly due to linear unsteady lift effects. The dynamic stall and wake theory significantly reduces the overpredictions of the quasisteady stall and dynamic stall theories and thereby improves the correlation. Overall, the dynamic stall and wake theory provides good correlation.

Figure 7 shows the calculated and measured damping levels for the fifth configuration with zero precone and shaft angle. The data are available for $0 \leq \mu \leq 0.187$ and show that the damping level monotonically increases with increasing advance ratio. This trend is captured by the dynamic stall and wake theory, although the calculated damping levels are low throughout. By comparison, the quasisteady stall and dynamic stall theories provide better correlation for $0 \leq \mu \leq 0.1$, but they do not continue to raise with advance ratio as do the data. Thus in summary, the dy-

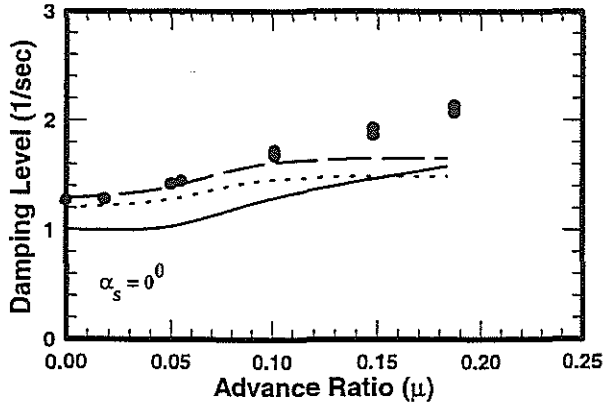


Figure 7: Lag Regressive-Mode Damping Correlation for $\theta_0 = 3^\circ$ and $\beta_{pc} = 0^\circ$ (Legend as in Fig. 5)

dynamic stall and wake theory provides fairly good correlation for this representative portion of the database on the lag regressive-mode damping except for the third configuration (Fig. 5c) for $\mu > 0.2$.

Thus far, in Figs. 5–7, we presented a comparison between the calculated and measured lag regressive-mode damping levels. Moreover, it is also important to assess the agreement between the calculations and the measurements for the trimmed equilibrium condition. During the experiment, the shaft angle, collective pitch, and advance ratio were set and the cyclic pitch angles were adjusted to provide minimum 1/rev flap bending moment at 12% radial station. Therefore, the cyclic pitch angles and steady root flap moment provide good measurements to assess the trimmed equilibrium solution. Unfortunately, the cyclic pitch measurements reported in Ref. 12 contained a phase error between the once per revolution signal and the root pitch angle signal. The cyclic pitch measurements reported in this paper are the corrected values. Given this background, the next six figures show the comparison of calculated and measured lateral-cyclic pitch θ_c (Figs. 8–10) and longitudinal cyclic pitch θ_l (Figs. 11–13); the first three configurations are covered in Figs. 8 and 11, the fourth in Figs. 9 and 12 and the fifth in Figs. 10 and 13. Figure 8 shows the comparison for the lateral cyclic pitch θ_c for $\alpha_s = 0^\circ, -3^\circ$ and -6° . The data show known trends: θ_c is zero at $\mu = 0.0$, increases suddenly around $\mu = 0.05$ and thereafter slowly decreases with increasing advance ratio. The rate of decrease is higher in Fig. 8c than in Figs. 8a and 8b. The calculations from the quasisteady stall and dynamic stall theories are nearly the same for all three configurations. They further show that the lateral cyclic pitch required to minimize 1/rev flapping moment is negative and that its magnitude monotonically increases with increasing advance ratio. Although these trends of the calculations are at best

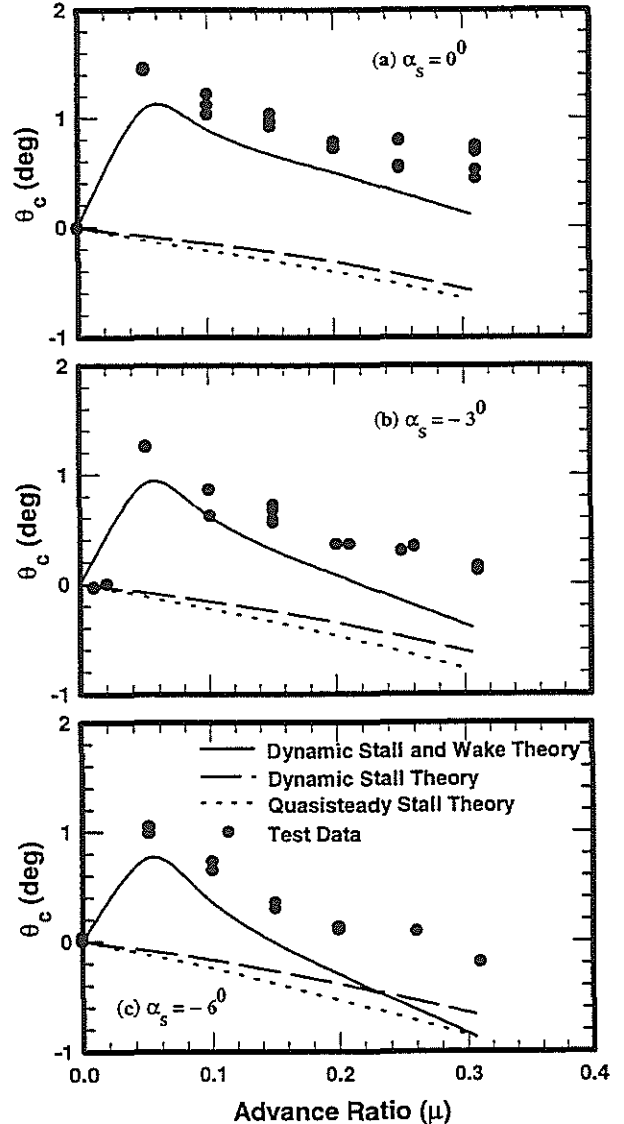


Figure 8: Lateral-Cyclic Pitch Correlation for $\theta_0 = 3^\circ$ and $\beta_{pc} = 2^\circ$

consistent with those of the data for $\mu \geq 0.05$, overall they are quantitatively inaccurate. But inclusion of wake effects dramatically improves the correlation, both quantitatively and qualitatively. In particular, the dynamic stall and wake theory predicts the sudden increase around $\mu = 0.05$; that is, in the transition regime when the flow over the rotor disk is associated with a large amount of shed and trailing vorticities. With increasing μ , the dynamic stall and wake theory captures the decreasing trend of the data. However, this rate of decrease is relatively higher and, hence, the calculation needs further examination for $\mu > 0.2$.

In Figs. 9 and 10, the data show a variation for θ_c similar to that in Fig. 8; that is, suddenly increasing at $\mu = 0.05$ and thereafter decreasing with increasing advance ratio. As seen from Figs. 9 and 10, both

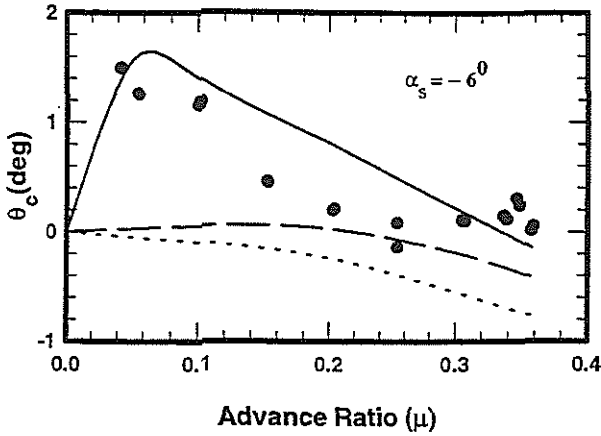


Figure 9: Lateral-Cyclic Pitch Correlation for $\theta_0 = 5.9^\circ$ and $\beta_{pc} = 2^\circ$ (Legend as in Fig. 8)

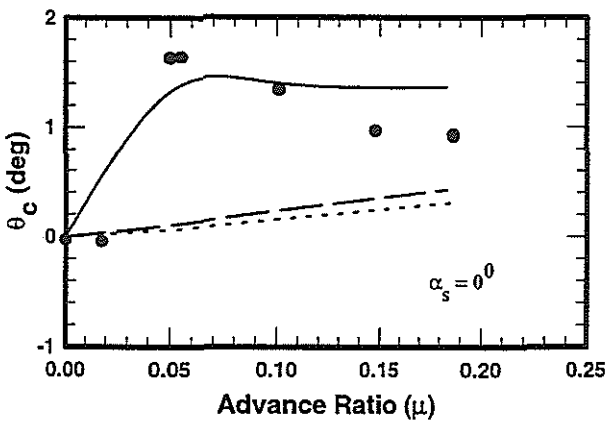


Figure 10: Lateral-Cyclic Pitch Correlation for $\theta_0 = 3^\circ$ and $\beta_{pc} = 0^\circ$ (Legend as in Fig. 8)

the dynamic stall and quasisteady stall theories fail to capture this variation and are not acceptable. By comparison, the dynamic stall and wake theory not only captures this variation but also provides fairly good correlation throughout.

In summary, Figs. 8–10 show that it is important to include wake effects in the calculation of lateral cyclic pitch angle θ_c and that the correlation in Fig. 8c merits further improvement at high speed conditions.

As seen from the data in Fig. 11, negative θ_s is required for the present trim condition of minimizing 1/rev root flapping moment. To fill in the details, we begin with Fig. 11a; the data show that θ_s is nearly zero up to $\mu \approx 0.05$ and that its magnitude increases with increasing μ thereafter. The calculations from the quasisteady stall and dynamic stall theories show that θ_s consistently increases with increasing μ , and the calculations from these two theories are nearly identical. Compared to the data, however, this rate of increase

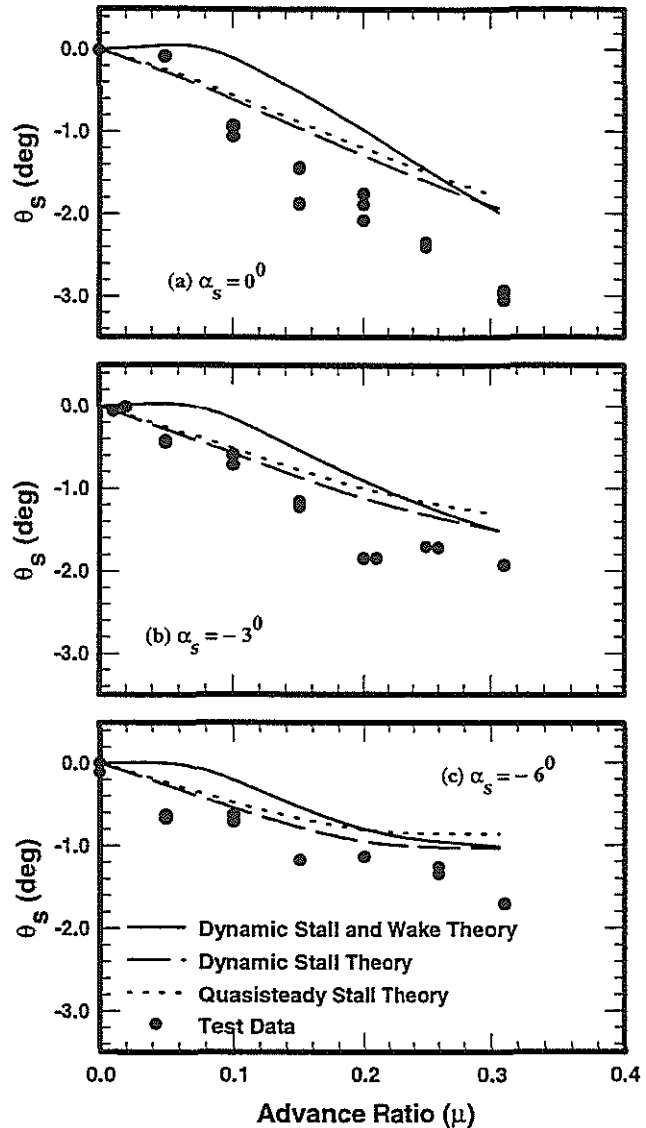


Figure 11: Longitudinal-Cyclic Pitch Correlation for $\theta_0 = 3^\circ$ and $\beta_{pc} = 2^\circ$

is lower. Moreover, for the first two configuration in Figs. 11a and 11b, these two theories fail to capture the finer details in the variations of θ_s with μ at very low advance ratios. By comparison, the dynamic stall and wake theory predicts that θ_s is nearly constant for $\mu \leq 0.075$ for all three configurations. Thereafter, however, it basically follows the other two theories.

The data in Figs. 12 and 13 show that the magnitude of θ_s increases with increasing advance ratio. The calculations from the quasisteady stall and dynamic stall theories are nearly identical and provide adequate correlation. The dynamic stall and wake theory slightly improves the correlation for the fourth configuration in Fig. 12 for $\mu > 0.25$ and for the fifth configuration in Fig. 13 for $\mu \leq 0.03$. But compared to the other

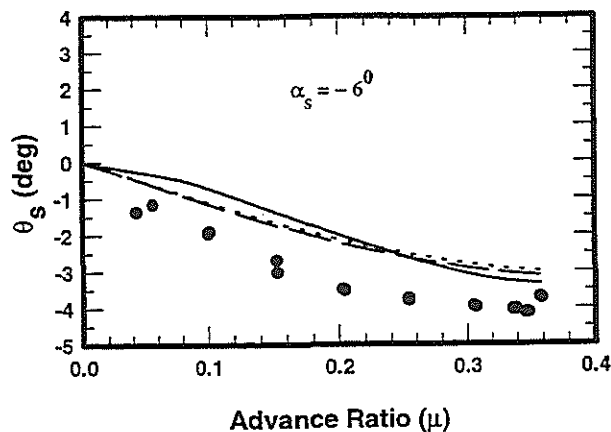


Figure 12: Longitudinal-Cyclic Pitch Correlation for $\theta_0 = 5.9^\circ$ and $\beta_{pc} = 2^\circ$ (Legend as in Fig. 11)

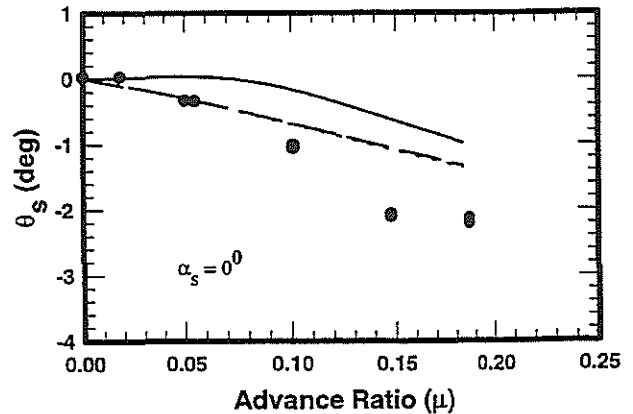


Figure 13: Longitudinal-Cyclic Pitch Correlation for $\theta_0 = 3^\circ$ and $\beta_{pc} = 0^\circ$ (Legend as in Fig. 11)

two theories, it also slightly overpredicts for $\mu < 0.25$ for the fourth configuration and for $\mu > 0.05$ for the fifth configuration.

Finally, Fig. 14 shows the comparison with the data for the steady flap moment at the 12% radial station. The force-integration method is used in Fig. 14a and the mode-deflection method in Fig. 14b. The flap-moment variation with advance ratio μ is well predicted by both methods in combination with each of the three theories. The thrust level C_T/σ is low throughout, which is 0.01 in hover, reaches a maximum value of 0.017 at $\mu = 0.15$ and thereafter reduces to zero at $\mu = 0.31$. Given such low-thrust conditions, the closeness of the calculations from the three theories is expected, and the dynamic stall and wake theory fares better than the other two theories. While the mode-deflection method fares better for $0 \leq \mu \leq 0.25$, the force-integration method fares better for $\mu > 0.25$. Despite the overall adequacy of the correlation, particularly by the mode-deflection method, there are appreciable differences between the calculations from these two methods, particularly at $\mu = 0.1$ and 0.31 . For example, relative to the data, the force integration and mode-deflection methods underpredict flap moment by 43% and 5% at $\mu = 0.1$ and overpredict by 10% and 30% at $\mu = 0.31$, respectively. Another point that merits mention is the convergence of the calculations based on 5-5-5 modal representation. Calculations have been made with 6-6-6 modal representation at $\mu = 0.1$ and 0.31 . The calculations from the force-integration method show little difference in steady flap moment from these two representations, and 5-5-5 representation basically provides converged results. However, the calculations from the mode-deflection method show a difference of 4.3% at $\mu = 0.1$ and 4% at $\mu = 0.31$, and the 6-6-6 modal representation brings the calculations closer to those of the force-integration method. Therefore, it is concluded

that the results in Fig. 14 merit further investigation concerning the differences in the calculations from the force-integration and mode-deflection methods as well as the convergence of the calculations from the mode-deflection method.

Concluding Remarks

The preceding correlation is based on the quasisteady stall, dynamic stall, and dynamic stall and wake theories. It covers the data on lag regressive-mode damping level, control settings of lateral and longitudinal pitch angles and steady root flap moment. All the data are presented as a function of advance ratio ($0 \leq \mu \leq 0.36$). Overall, the dynamic stall and wake theory provides the best correlation. The other specific findings are as follows:

1. The quasisteady stall and dynamic stall theories predict the damping levels fairly well. By comparison, the dynamic stall and wake theory shows better correlation in that the trend of the damping level with advance ratio is closer to that of the data. An exception occurs for the third configuration for $0.2 \leq \mu \leq 0.31$; the data show that the damping level rapidly decreases for $\mu > 0.2$ and becomes nearly zero at $\mu = 0.31$. This is predicted by none of the three theories. They predict nearly identical damping for $0.2 \leq \mu \leq 0.31$ and show that the damping level decreases very slowly with increasing advance ratio; in fact, they predict a fairly stable lag regressive mode at $\mu = 0.31$. That this exception occurs under near-zero thrust conditions ($0.017 \leq C_T/\sigma \leq 0.0$) is surprising and merits further investigation.
2. The quasisteady stall and dynamic stall theories do not provide a satisfactory correlation of the lat-

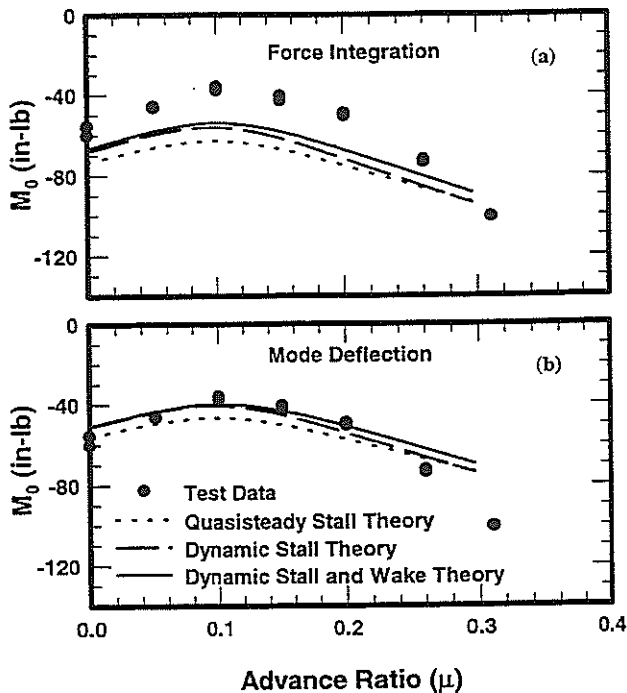


Figure 14: Flapping Moment Correlation for $\theta_0 = 3^\circ$, $\alpha_s = -6^\circ$ and $\beta_{pc} = 2^\circ$

eral cyclic pitch angle. In contrast, the dynamic stall and wake theory dramatically improves the correlation and provides satisfactory correlation.

3. The calculations of the root flap moment from all three theories are fairly close. The mode-deflection method correlates better than the force-integration method. However, two issues concerning the convergence of the calculations from the mode-deflection method with respect to the number of modes, and the differences in the calculations from the mode-deflection and force-integration methods must be resolved.

Acknowledgment

This work is sponsored by Army Research Office under Grant DAAL03-91-G-0007 and DAAH04-94-G-00185, and Army Aeroflightdynamics Directorate (AFDD) at Ames Research Center under Grant NAG-2-797. The authors are grateful to Dr. R. A. Ormiston, who took keen interest during the progress of this work and made several useful suggestions.

References

1. McNulty, M. J., "Flap-Lag Stability Data for a Small Scale Isolated Hingeless Rotor in Forward Flight," NASA TM 102189, Apr 1989.

2. Gaonkar, G. H., McNulty, M. J. and Nagabushanam, J., "An Experimental and Analytical Investigation of Isolated Rotor Flap-Lag Stability in Forward Flight," *Journal of the American Helicopter Society*, Vol. 35, (2), Jun 1990, pp 25-34.
3. Barwey, D., Gaonkar, G. H. and Ormiston, R. A., "Investigation of Dynamic Stall Effects on Isolated Rotor Flap-Lag Stability with Experimental Correlation," *Journal of the American Helicopter Society*, Vol. 36, (4), Oct 1991, pp 12-24.
4. Torok, M. S. and Chopra, I., "Hingeless Rotor Aeroelastic Stability Analysis With Refined Aerodynamic Modeling," *Journal of the American Helicopter Society*, Vol. 36, (4), Oct 1991, pp 48-56.
5. Barwey, D. and Gaonkar, G. H., "Dynamic-Stall and Structural-Modeling Effects on Helicopter Blade Stability with Experimental Correlation," *AIAA Journal*, Vol. 32, (4), Apr 1994, pp 811-819.
6. Subramanian, S., *Dynamic Stall and Three-Dimensional Wake Effects on Trim and Stability of Isolated Rotors with Experimental Correlation and Parallel Fast-Floquet Analysis*, Ph. D. Thesis, College of Engineering, Florida Atlantic University, Boca Raton, FL, Aug 1996.
7. Tang, D. M. and Dowell, E. H., "Damping Prediction for a Stalled Rotor in Flap-Lag with Experimental Correlation," *Journal of the American Helicopter Society*, Vol. 40, (4), Oct 1995, pp 79-89.
8. Chunduru, S., Subramanian, S. and Gaonkar, G. H., "Dynamic Stall and Wake Effects on Trim and Stability of Hingeless Rotors with Experimental Correlation," Vol. 42, (4), Oct 1997 (to appear). (Also see the proceedings of the 50th Annual Forum of the American Helicopter Society, Washington, D.C., May 11-13, 1994.)
9. de Andrade, D., da Silva Correa, M. and Peters, D. A., "New Correlation of Experimental Flap-Lag-Torsion Damping," Proceedings of the 52nd Annual Forum of the American Helicopter Society, Washington, D.C., Jun 4-6, 1996.
10. Cho, M. H., Jeon, S. M., Woo, S. H. and Lee, I., "Refined Aeroelastic Analysis of Hingeless Rotor Blades in Hover," *Journal of Aircraft*, Vol. 34, (2), May-June 1997, pp 408-415.
11. Sharpe, D. L., "An Experimental Investigation of the Flap-Lag-Torsion Aeroelastic Stability of a Small Scale Hingeless Rotor in Hover," NASA TP 2546, Aviation Systems Command (AVSCOM) TR 85-A-9, 1986.

12. Maier, T. H., Sharpe, D. L. and Lim, J., "Fundamental Investigation of Hingeless Rotor Aeroelastic Stability, Test Data and Correlation," Proceedings of the American Helicopter Society 51st Annual Forum, Forth Worth, TX, May 9-11, 1995.
13. Tang, D. and Dowell, E. H., "Damping Prediction for Hingeless Rotor Aeroelastic Stability with Experimental Correlation" *Journal of Aircraft*, Vol. 33, (6), Nov-Dec 1996, pp 1071-1078.
14. Tang, D. and Dowell, E. H., "Hingeless Rotor Aeroelastic Stability with Dynamic Stall and Advanced Wake," Private communication, Nov 8, 1996.
15. Peters, D. A., "Toward a Unified Lift Model for Use in Rotor Blade Stability Analysis," *Journal of the American Helicopter Society*, Vol. 30, (3), Jul 1985, pp 32-42.
16. Petot, D., "Differential Equation Modeling of Dynamic Stall," ONERA, Technical Note No. 5, 1989.
17. Peters, D. A., Boyd, D. D. and He, C. J., "Finite-State Induced-Flow Model for Rotors in Hover and Forward Flight," *Journal of the American Helicopter Society*, Vol. 34, (4), Oct 1989, pp 5-17.
18. Critzos, C. C., Heyson, H. H. and Boswinkle, Jr., R. W., "Aerodynamic Characteristics of NACA 0012 Airfoil Section at Angles of Attack from 0° to 180° ," NACA Tech Note 3361, Jan 1965.
19. Bielawa, R. L., "Blade Stress Calculation — Mode Deflection vs. Force Integration," *Journal of the American Helicopter Society*, Vol. 23, (2), Apr 1978, pp 10-16.